Environmental Science & Technology

pubs.acs.org/est

Article

Fe−Fe Double-Atom Catalysts for Murine Coronavirus Disinfection: Nonradical Activation of Peroxides and Mechanisms of Virus Inactivation

Zhe Zhou, Mengqiao Li, Yuxin Zhang, Lingchen Kong, Virginia F. Smith, Mengyang Zhang, Anders J. Gulbrandson, Gordon H. Waller, Feng Lin, Xitong Liu, David P. Durkin,* Hanning Chen,* and Danmeng Shuai*

Cite This: https://doi.org/10.1021/acs.est.3c00163

Read Online

ACCESS | Metrics & More | Article Recommendations | Supporting Information

ABSTRACT: Peroxides find broad applications for disinfecting environmental pathogens particularly in the COVID-19 pandemic; however, the extensive use of chemical disinfectants can threaten human health and ecosystems. To achieve robust and sustainable disinfection with minimal adverse impacts, we developed Fe single-atom and Fe−Fe double-atom catalysts for activating peroxymonosulfate (PMS). The Fe−Fe double-atom catalyst supported on sulfur-doped graphitic carbon nitride outperformed other catalysts for oxidation, and it activated PMS likely through a nonradical route of catalyst-mediated electron transfer. This Fe−Fe double-atom catalyst enhanced PMS disinfection kinetics for inactivating murine coronaviruses (i.e., murine hepatitis virus strain A59 (MHV-A59)) by 2.17−4.60 times when compared to PMS treatment alone in diverse environmental media including simulated saliva and freshwater. The molecular-level mechanism of MHV-A59 inactivation was also elucidated. Fe−Fe double-atom catalysis promoted the damage of not only viral proteins and genomes but also internalization, a key step of virus lifecycle in host cells, for enhancing the potency of PMS disinfection. For the first time, our study advances double-atom catalysis for environmental pathogen control and provides fundamental insights of murine coronavirus disinfection. Our work paves a new avenue of leveraging advanced materials for improving disinfection, sanitation, and hygiene practices and protecting public health.

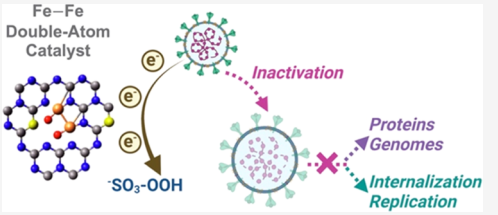

KEYWORDS: *double-atom catalyst, catalyst-mediated electron transfer, murine coronavirus, disinfection, peroxymonosulfate*

INTRODUCTION

Devastating disease outbreaks, epidemics, and pandemics have resulted from environmental transmission of enveloped viruses, such as influenza A virus, Marburg virus, Ebola virus, severe acute respiratory syndrome coronaviruses 1 and 2 (SARS-CoV-1 and SARS-CoV-2), Middle East respiratory syndrome coronavirus, and monkeypox virus.[1−3] Enveloped viruses can spread between humans via direct and indirect contacts through respiratory droplets, aerosols, fomites, and so on.[4,5] Although the waterborne transmission of enveloped viruses between humans has not been validated,[6] some enveloped viruses such as avian influenza A virus and swine acute diarrhea syndrome coronavirus primarily transmit via the fecal−oral route between animals, and the feces of infected animals could lead to the zoonotic spillover of these viruses to humans through water and fomites.[7−9] In addition, enveloped viruses can survive in water and inanimate surfaces up to a few days at room temperature.[5,10] To minimize the environmental transmission of enveloped viruses and prevent the spread of infectious diseases, disinfection has been widely adopted.[11] For example, the U.S. Environmental Protection Agency recommends more than 500 disinfectants that are effective against SARS-CoV-2.[11] However, the excessive use of disinfectants has negative impacts on human health and ecosystems.[11] Therefore, there is an urgent need for advancing effective, robust, and sustainable disinfection to inactivate enveloped viruses while minimizing the deleterious effects of disinfectants.

Peroxides such as hydrogen peroxide, persulfate, and peracetic acid have been extensively applied as water disinfectants and/or surface sanitizers.[11−13] However, some peroxides (i.e., hydrogen peroxide and persulfate) are generally less effective in inactivating pathogens when compared to highly reactive disinfectants like free chlorine and ozone, and a high concentration of peroxides and a long contact time are often needed to achieve desired disinfection performance.[12,14,15] Fortunately, peroxides can be activated through catalysis to produce a broad spectrum of reactive species, and their microbicidal potency is significantly enhanced. Heterogeneous single-atom catalysts, which integrate the advantages

Received: January 6, 2023
Revised: February 5, 2023
Accepted: February 7, 2023

of typical homogeneous and heterogeneous catalysts such as well-defined mononuclear metal-active sites, high stability, and easy separation for different applications, have been found to activate peroxides for degrading chemical contaminants effectively by producing radicals (e.g., hydroxyl radical ($^{\bullet}OH$)),[16] singlet oxygen ($^1O_2$),[17] and high-valent metal−oxo species,[18] or facilitating electron transfer through the catalyst in peroxide reduction.[19] Notably, catalyst-mediated electron transfer enables rapid and complete chemical pollutant oxidation, minimized toxic byproduct formation, and (near) stoichiometric oxidant consumption.[20−22] Previous discoveries of the unique catalyst-mediated electron-transfer mechanism on single-atom catalysts have laid a solid foundation for rapid, resilient, and environmentally and human health benign virus inactivation. As a breakthrough beyond single-atom catalysts, double-atom catalysts inherit the advantages of single-atom catalysts originating from the atomically dispersed nature, and their isolated, dual-metal-atom pairs can further enhance the catalytic performance. By introducing an additional neighboring metal atom to the metal center of single-atom catalysts, the geometric and electronic structure of the catalysts is modified, additional reactions sites are offered, and the interactions of reactants and intermediates with the catalysts are optimized.[23]

The goal of our study is to advance single-atom and double-atom catalysis for disinfecting enveloped viruses and elucidate the mechanism of virus inactivation. Inspired by the thiolate-ligated heme-iron center in cytochrome P450, we developed Fe single-atom and Fe−Fe double-atom catalysts supported on pristine and sulfur (S)-doped graphitic carbon nitride because simply doping with heteroatoms such as S in the catalyst structure would influence the electronic structure of the center single- and double-atom metals for boosting corresponding catalytic activity.[24] Using phenol as a probe compound, we identified that Fe−Fe double-atom catalysts outperformed their counterpart of Fe single-atom catalysts, and the Fe−Fe double-atom catalyst supported on S-doped graphitic carbon nitride had the best oxidation performance by activating PMS. We then selected murine coronavirus (i.e., MHV-A59) as a representative enveloped virus to investigate disinfection performance of PMS-alone and Fe−Fe double-atom catalyst-activated PMS treatments. Simulated saliva and freshwater were used as typical environmental matrices to mimic contact surface cleaning and water disinfection, respectively. PMS-driven disinfection mechanisms were systematically evaluated by both experimental and computational approaches, including the molecular-level damage of viral genomes, proteins, and lipids, as well as the murine coronavirus lifecycle in host cells. When compared to PMS disinfection alone, Fe−Fe double-atom catalysis likely promoted catalyst-mediated electron transfer and induced damage to viral genomes, proteins, and internalization into host cells for enhanced disinfection. In our study, for the first time, double-atom catalysis was developed and implemented for environmental pathogen control and the mechanisms of murine coronavirus disinfection by PMS-driven treatments were evaluated at the molecular level. Research discoveries of our work can find broad engineering applications for advancing catalysis in pollution control, enabling effective and safe disinfection, controlling the environmental transmission of pathogens, and ultimately protecting public health.

MATERIALS AND METHODS

Chemicals and Reagents. Details of all chemicals and reagents are listed in Text S1. They were used as received without any treatment.

Material Synthesis and Characterization. Fe single-atom and Fe−Fe double-atom catalysts supported on pristine graphitic carbon nitride (CN) and S-doped graphitic carbon nitride (SCN) were prepared by thermal polycondensation, i.e., an Fe single-atom catalyst supported on CN (Fe/CN), an Fe single-atom catalyst supported on SCN (Fe/SCN), an Fe−Fe double-atom catalyst supported on CN (Fe−Fe/CN), and an Fe−Fe double-atom catalyst supported on SCN (Fe−Fe/SCN). Briefly, iron (III) nitrate nonahydrate ($Fe(NO_3)_3\cdot 9H_2O$) or an Fe_2 dimer precursor (cyclopentadienyliron dicarbonyl dimer, $Fe_2(CO)_4(C_5H_5)_2$) was loaded on the supramolecules of cyanuric acid−melamine or trithiocyanuric acid−melamine and subjected to pyrolysis at 500 °C for 4 h under a flow of nitrogen. SCN was also prepared from trithiocyanuric acid-melamine as a control. Details of material synthesis and characterization are shown in Texts S2 and S3.

MHV-A59 Inactivation by PMS-Alone and Fe−Fe Double-Atom Catalysis. MHV-A59 stock was prepared according to our previous publications (Text S4), and the viral concentration was ca. 10^{10} gene copies mL^{-1}. MHV-A59 inactivation by PMS-alone and Fe−Fe/SCN-activated PMS (Fe−Fe/SCN + PMS) treatment was evaluated in three different matrices, including a model phosphate buffer (pH 7, 10 mM), simulated saliva, and freshwater collected from the Potomac River (provided by a local drinking water treatment facility). The preparation of simulated saliva with mucin was based on the ASTM E2720 standard,[25] and saliva components are included in Table S1. Freshwater quality parameters are provided in Table S2. For Fe−Fe/SCN-activated PMS disinfection, MHV-A59 stock was spiked in different matrices to reach a viral concentration of ca. 10^8 gene copies mL^{-1}, mixed with the catalyst for 20 min at room temperature to reach the adsorption equilibrium, and amended with PMS to initiate MHV-A59 inactivation. Samples were withdrawn at different time intervals, immediately quenched by the same volume of $Na_2S_2O_3$ (10 mM), and centrifuged at 2000 × g for 30 s to spin down the catalyst. The supernatant was collected and stored at 4 °C for the viral infectivity assay. For MHV-A59 inactivation by PMS alone, a similar protocol was used but the amendment and separation of the catalyst were not needed. The PMS concentration was determined using the colorimetric method with 2,2′-azino-bis(3-ethylbenzothiazoline-6-sulfonic acid) diammonium salt (ABTS) using a UV−vis spectrophotometer (GENESYS 150) (Text S5).

Viral Infectivity Assay. The integrated cell culture−reverse transcription−quantitative polymerase chain reaction (ICC-RT-qPCR) assay which combines cell culture with targeted viral genome detection by qPCR was employed to determine the loss of MHV-A59 infectivity during disinfection in a timely and specific manner (Text S6).[26] Synthetic cDNA oligos (Integrated DNA Technologies, Inc.) were prepared in a series of 10-fold dilutions (10^3−10^{12} gene copies mL^{-1}) to generate the standard curve of absolute gene copy numbers versus cycle threshold values. In our RT-qPCR protocol, 5 μL of the RNA template was added to 5 μL of TaqMan fast virus one-step master mix (Fisher Scientific, Applied Biosystems 4444434), 2 μL of forward primer (10 μM), 2 μL of reverse primer (10 μM), 1.25 μL of probe (10 μM), and 4.75 μL of

https://doi.org/10.1021/acs.est.3c00163
Environ. Sci. Technol. XXXX, XXX, XXX−XXX

nuclease-free water, following cycling conditions of 52 °C for 10 min (reverse transcription), 95 °C for 20 s (reverse transcription inactivation and denaturation initiation), and 45 cycles of 95 °C for 15 s and 60 °C for 1 min. Detailed sequence information is provided in Table S3. Quantitative polymerase chain reaction efficiency for MHV-A59 in this study was 87.1−104.7%, and its coefficient of determination was 0.994−0.999. Serial dilutions of extracted RNA from MHV-A59 stock did not indicate any inhibition for RT-qPCR (Table S4). All RT-qPCR data are reported following MIQE guidelines.[27] A linear relationship was observed between MHV-A59 infectivity determined by ICC-RT-qPCR and the viral load before infection quantified by RT-qPCR (Figure S1), indicating the validity of the ICC-RT-qPCR assay for quantifying the viral infectivity. Notably MHV-A59 infectivity only above $\sim 10^8$ gene copies well^{-1} was quantifiable (Figure S1) in our study. MHV-A59 infectivity in disinfection followed pseudo-first-order decay

$$\log_{10}\text{ inactivation} = \log_{10}\left(\frac{N_0}{N_t}\right) = 0.434 \times k_{\text{infectivity}} \times t$$

where N_t and N_0 are the genome copy number per well of disinfected MHV-A59 at time t (min) and untreated MHV-A59 at time zero as measured by ICC-RT-qPCR, respectively, and $k_{\text{infectivity}}$ is the pseudo-first-order inactivation rate constant of MHV-A59. At least triplicates were conducted for each experiment, and the mean and standard deviation are reported. The CT values (mg min L^{-1}) for 1-log$_{10}$, 2-log$_{10}$, and 3-log$_{10}$ inactivation of MHV-A59 were calculated by the following equation

$$\text{CT} = \int_0^t C\, dt$$

where C (mg L^{-1}) is the concentration of PMS, t (min) is the contact time, and the integral represents the area under the PMS consumption curve up to a certain time point when 1-log$_{10}$, 2-log$_{10}$, and 3-log$_{10}$ inactivation of MHV-A59 were achieved, respectively.

Damage of Biomolecules and Lifecycle of MHV-A59 during Virus Inactivation. The damage of MHV-A59 genomes, proteins, and lipids and MHV-A59 lifecycle in host cells, including binding and internalization, after disinfection was characterized quantitatively. Following the same protocol of MHV-A59 disinfection in the phosphate buffer (pH 7, 10 mM), disinfected viral samples were collected at different time intervals, and the reaction was quenched by $Na_2S_2O_3$.

For the genome damage analysis, viral RNA was extracted from samples using the Quick-RNA viral kit (Zymo research, R1035) and then proceeded to RT-qPCR. The pseudo-first-order reaction rate constant for viral genome damage ($k_{\text{genome damage}}$) was obtained from the negative slope of the linear regression of the natural logarithm of genome copy numbers versus time. At least triplicates were conducted for each experiment, and the mean and standard deviation are reported. For protein and lipid damage analysis, MHV-A59 stock was first purified through ultracentrifugation prior to disinfection to remove the impurities like free amino acids and small cell debris in the virus stock and eliminate their interference in protein and lipid oxidation assays (Text S7). Next, purified MHV-A59 was disinfected, and the protein concentration of disinfected viruses was determined using the Pierce BCA protein assay kit (Thermo Fisher, 23227, the enhanced protocol was used following manufacturer's manual). The protein carbonyl content of disinfected viruses was measured using the OxiSelect protein carbonyl enzyme-linked immunosorbent assay (ELISA) kit (Cell Biolabs, STA-310), and the content of malondialdehyde (MDA), a lipid oxidation byproduct, was quantified using the OxiSelect MDA adduct competitive ELISA kit (Cell Biolabs, STA-832). Particularly, prior to the protein carbonyl ELISA, viruses after disinfection were first lysed by ultrasonication in a mixture of 10 mM phenylmethylsulfonyl fluoride (PMSF) and 0.05 wt % butylated hydroxytoluene (BHT),[28] and then, the lysed viruses were diluted to 10 μg of protein mL^{-1} as determined by the Pierce BCA protein assay. Prior to the MDA adduct ELISA assay, disinfected MHV-A59 was also ultrasonicated in PMSF-BHT for lysis. The linear relationship between the protein concentration of the serially diluted, purified MHV-A59 stock and the dilution factor demonstrated the validity of the Pierce BCA protein assay (Table S5). The pseudo-first-order reaction rate constant for viral protein damage was obtained from the negative slope of the linear regression of the natural logarithm of protein concentrations measured by the BCA protein assay versus time. At least duplicates were conducted for each experiment, and the mean and standard deviation are reported.

For MHV-A59 binding to and internalization into host cells, disinfected MHV-A59 was incubated with L-929 cells at two different temperatures (i.e., 4 and 37 °C) for subsequent RT-qPCR quantification (Text S8). Incubating MHV-A59 with host cells at 4 °C only allows virus binding, but a subsequent increase of the incubation temperature to 37 °C permits virus internalization.[29] The pseudo-first-order reaction rate constants for the viral genome loss measured in virus binding and internalization assays ($k_{\text{observed binding}}$ and $k_{\text{observed internalization}}$), respectively, were obtained from the negative slope of the linear regression of the natural logarithm of genome copy numbers versus time. The true damage to virus binding and internalization rate constants were corrected as $k_{\text{binding}} = k_{\text{observed binding}} - k_{\text{genome damage}}$ and $k_{\text{internalization}} = k_{\text{observed internalization}} - k_{\text{observed binding}}$ to exclude the PCR signal decrease due to the damage of viral genomes and virus binding (observed) in the same treatment, respectively.[30] At least triplicates were conducted for each experiment, and the mean and standard deviation are reported.

Computational Simulation Methods. Aiming to provide fundamental understanding of Fe−Fe double-atom catalysis for oxidizing MHV-A59 proteins and genomes and impairing virus lifecycle, we also applied computational simulations to study the interaction of Fe−Fe/SCN with PMS and with representative amino acids and a representative nucleobase. Simulations were performed by the open-source CP2K software[31] with the HSE06 exchange−correlation functional,[32] the Goedecker−Teter−Hutter (GTH) pseudopotential,[33] the polarized valence double-zeta (pVDZ) basis set,[34] and an implicit aqueous solvation model.[35] In addition, the constrained density functional theory (CDFT)[36] was employed to model the oxidation reactions' initial and final diabatic states and their electronic coupling strength according to the block-diagonalization formula.[37] More specifically, a position-dependent Hartree potential was added to the system's Hamiltonian to enforce a total density-derived atomic partial charge (DDAPC)[38] of zero on the amino acid or nucleobase at its initial diabatic state, while a total DDAPC charge of +1 was imposed by the same approach at its final diabatic state upon oxidation. More specifically, the Broyden−Fletcher−Gold-

https://doi.org/10.1021/acs.est.3c00163
Environ. Sci. Technol. XXXX, XXX, XXX−XXX

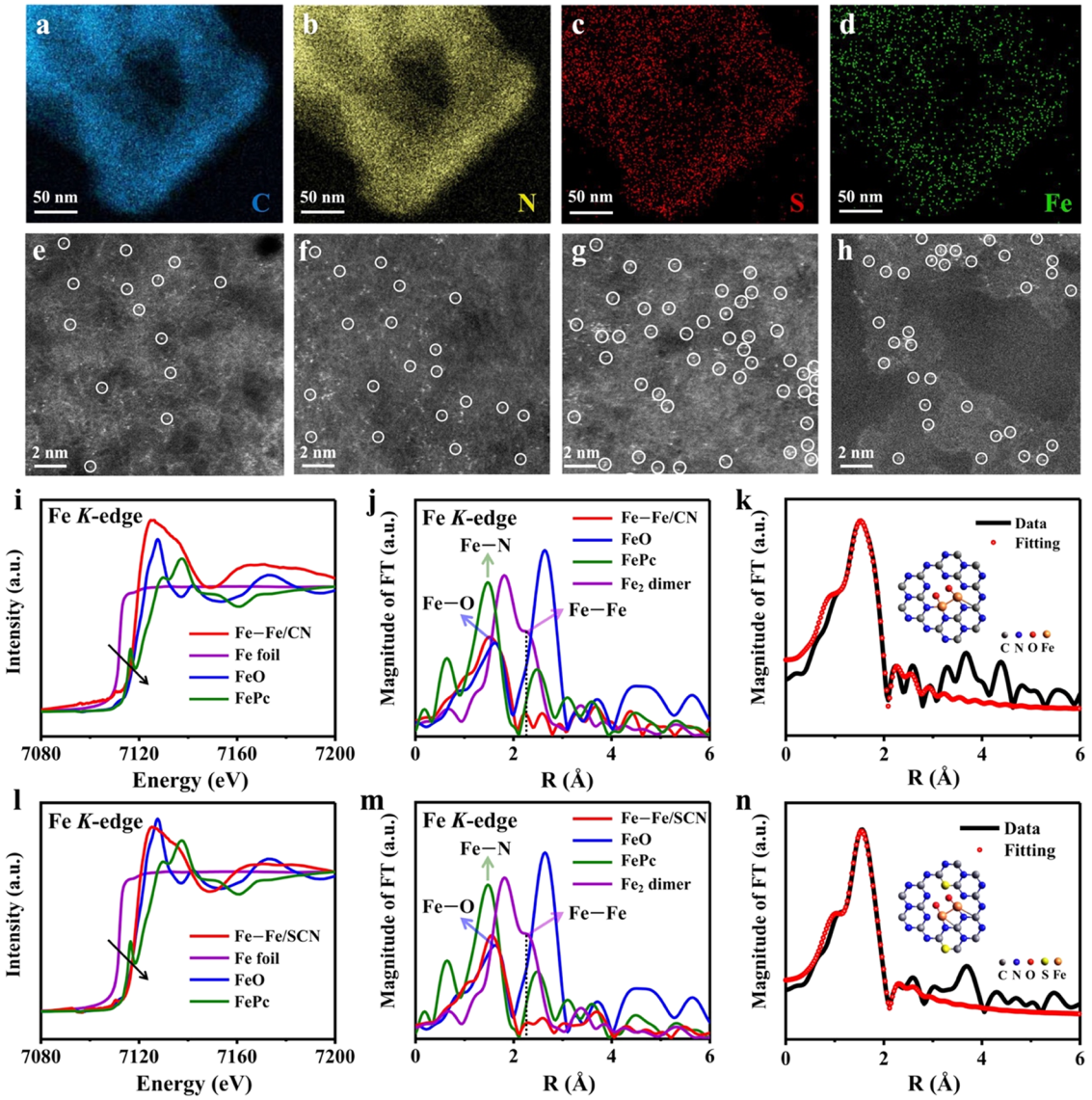

Figure 1. Characterization of Fe single-atom and Fe−Fe double-atom catalysts. (a−d) Scanning transmission electron microscopy (STEM) elemental distribution of C, N, S, and Fe elements in Fe−Fe/SCN. AC-HAADF-STEM images of (e) Fe/CN, (f) Fe/SCN, (g) Fe−Fe/CN, and (h) Fe−Fe/SCN. The normalized XANES spectra and the FT k^3-weighted EXAFS spectra at Fe *K*-edge of (i, j) Fe−Fe/CN, (l, m) Fe−Fe/SCN, and reference materials (i.e., FeO, FePc, and Fe_2 dimer of cyclopentadienyliron dicarbonyl dimer). EXAFS experimental data and *R*-space fitting of (k) Fe−Fe/CN and (n) Fe−Fe/SCN. The insets are fitted structures.

farb−Shanno (BFGS) algorithm[39] was applied to optimize the geometries of the initial and final diabatic states until the four following convergence criteria were simultaneously met: the maximum force component was less than 4.5×10^{-4} Hartree $Bohr^{-1}$; the root-mean-square force component was less than 3.0×10^{-4} Hartree $Bohr^{-1}$; the maximum geometry change was less than 3.0×10^{-3} Bohr; the root-mean-square geometry change was less than 1.5×10^{-3} Bohr. Once an optimized geometry had been ascertained, its energy was iteratively evaluated by the directive inversion in the iterative subspace (DIIS) approach[40] in conjunction with the orbital transformation (OT) method[41] until the electron density change was less than 1.0×10^{-8} per Bohr.[3] The same protocol of geometry optimization and energy evaluation was adopted when we calculated the adsorption energy of our model systems, each of which consisted of a 6 × 6 heptazine-based substrate and an adsorbent (Figure S2).

Statistical Analysis. Student's *t*-test and the analysis of covariance were applied for the statistical comparison of MHV-A59 infectivity and disinfection kinetics and the damage rate constant of viral biomolecules and lifecycle under different treatments, which returned to a *p* value. All *p* values smaller than 0.05 were considered statistically significant.

RESULTS AND DISCUSSION

Characterization of Fe Single-Atom and Fe−Fe Double-Atom Catalysts. X-ray diffraction (XRD) patterns of all as-synthesized catalysts (i.e., Fe/CN, Fe−Fe/CN, Fe/SCN, and Fe−Fe/SCN) displayed in Figure S3 showed two main diffraction peaks at around 13 and 27°, attributing to the (100) and (002) planes of graphitic carbon nitride.[42−44] Particularly, no characteristic peaks of Fe were observed in XRD patterns, suggesting the absence of crystalline Fe-bearing particles in the catalysts.[24,43] The transmission electron microscopy (TEM) images of the representative Fe−Fe/

https://doi.org/10.1021/acs.est.3c00163
Environ. Sci. Technol. XXXX, XXX, XXX−XXX

SCN in Figure S4 first revealed that no particles or clusters were observed on the entire graphitic carbon nitride matrix, suggesting that all Fe species might atomically exist in the catalyst structure. The elemental mappings in Figures 1a−d and S5 revealed the homogeneous distribution of C, N, O, S, and Fe across the entire catalyst. The Fe loading of Fe/CN, Fe−Fe/CN, Fe/SCN, and Fe−Fe/SCN was 0.65, 0.49, 0.43, and 0.45 wt %, respectively, as determined by inductively coupled plasma−optical emission spectroscopy (ICP-OES) (Table S6). To confirm the singly dispersed Fe atoms on Fe/CN and Fe/SCN and the double-atomic feature of Fe species on Fe−Fe/CN and Fe−Fe/SCN, aberration-corrected high-angle annular dark-field scanning transmission electron microscopy (AC-HAADF-STEM) was used to characterize the catalyst samples. The AC-HAADF-STEM images of Fe/CN and Fe/SCN in Figure 1e,f showed a large number of bright dots spreading in the graphitic carbon nitride support, which corresponded to the atomically dispersed single Fe atoms.[24] For Fe−Fe/CN and Fe−Fe/SCN samples, many paired dots were observed in the AC-HAADF-STEM images (Figure 1g,h), which were consistent with the feature of two adjacent Fe atoms. Since the AC-HAADF-STEM imaging only represents a two-dimensional projection of the three-dimensional Fe−Fe/CN and Fe−Fe/SCN samples along the incident beam direction, the appearances of the paired dots were different depending on the orientation of the Fe−Fe bond; additionally, the isolated bright dots were also observed in the AC-HAADF-STEM images of Fe−Fe/CN and Fe−Fe/SCN samples (Figure 1g,h), and we attributed them to the overlapping of two Fe atoms in the incident beam direction or/and the incomplete imaging of the double-atom Fe species.[43,45] The statistical analysis of 75 paired dots exhibited in the AC-HAADF-STEM images of Fe−Fe/CN and Fe−Fe/SCN samples showed that the projected Fe−Fe distance was about 2.3 ± 0.4 and 2.3 ± 0.7 Å, respectively (Table S7).

The attenuated total reflectance−Fourier transform infrared (ATR-FTIR) spectra (Figure S6) showed the typical structure of graphitic carbon nitride in all catalysts with absorption bands near 3177, 1650−1200, and 806 cm^{-1}, corresponding to the stretching vibration of N−H bonds, C−NH−C and N−$(C)_3$ bonds, and the tri-*s*-triazine units, respectively.[44] X-ray photoelectron spectroscopy (XPS) was used to evaluate the bonding environment and oxidation state of surface elements (ca. 10 nm) in the catalysts. The C(1s) region of Fe−Fe/SCN (Figure S7c) deconvoluted into three peaks at 284.5, 287.5, and 293.1 eV, corresponding to C−H/C−S, N−C═N, and $\pi-\pi$ stacking, respectively; these three peaks were also observed in the C(1s) region of Fe−Fe/CN (Figure S7b); however, for Fe−Fe/CN, the peak at 284.5 eV was only assigned to C−H bonds.[42] The N(1s), O(1s), and Fe(2p) regions for Fe−Fe/CN and Fe−Fe/SCN were also quite similar (Figure S7b,c). The N(1s) region deconvoluted into three peaks at 398.0, 399.4, and 404.2 eV and were assigned to C−N═C, N−$(C)_3$, and $\pi-\pi$ stacking, respectively.[42] The single broad peak in the O(1s) region centered at 531.9 eV was most likely due to a mixture of organic oxides (C−O, etc.) on the edges of the catalyst structure and/or some metal oxide species. Although the Fe concentration was quite low, a weak doublet ($Fe(2p_{1/2}/2p_{3/2})$) could be discerned in the Fe(2p) region of Fe−Fe/SCN (Figure S7c); the $Fe(2p_{3/2})$ peak at 709.6 eV suggested that the Fe species existed only in an oxidized form. Interestingly, no differences were observed in the S(2p) spectra of SCN and Fe−Fe/SCN (Figure S7a,c); the presence of a $S(2p_{3/2}/2p_{1/2})$ doublet with the $2p_{1/2}$ centered at 163.4 eV was assigned to the sulfide species (C−S−C) within the graphitic carbon nitride substrate.[24] These data suggested that Fe was less likely to coordinate with S in the catalyst. To clearly demonstrate the local coordination environment and the oxidation state of Fe at the atomic level, X-ray absorption spectroscopy (XAS) was performed. The X-ray absorption near-edge structure (XANES) spectra of catalysts and reference samples (i.e., Fe foil, iron (II) oxide (FeO), and iron(II) phthalocyanine (FePc)) at *K*-edge (Figures 1i,l, and S8) revealed that the absorption edge of Fe/CN, Fe−Fe/CN, Fe/SCN, and Fe−Fe/SCN was located at the position coincided with FeO and FePc, indicating that the valence state of Fe species in all catalysts was close to 2+, which was in agreement with the XPS data. The Fourier transform (FT) k^3-weighted extended X-ray absorption fine structure (EXAFS) spectrum of the Fe_2 dimer precursor shown in Figure 1j displayed a peak at 2.27 Å, corresponding to the Fe−Fe coordination path.[43] Figures 1j,m and S9 showed the FT k^3-weighted EXAFS spectrum of Fe/CN, Fe−Fe/CN, Fe/SCN, and Fe−Fe/SCN with a broad peak centered at 1.60, 1.50, 1.69, and 1.56 Å, respectively, attributable to Fe−N/O coordination in the catalyst structure (Fe−N path at 1.50 Å from FePc and Fe−O path at 1.63 Å from FeO, Figure 1j). Additionally, no characteristic peak of Fe−Fe (at 2.27 Å) was observed in Fe/CN and Fe/SCN (Figure S9), demonstrating that Fe atoms were single-atomically dispersed on the catalyst support. For Fe/SCN and Fe−Fe/SCN that were prepared on the SCN support, no characteristic peak of Fe−S (at 1.80 Å) was observed in their EXAFS spectra (Figures 1m and S9b),[24] indicating that Fe atoms did not coordinate with S in the graphitic carbon nitride matrix. The EXAFS spectra of Fe−Fe/CN and Fe−Fe/SCN, which were prepared from the Fe_2 dimer precursor exhibited a secondary peak located at 2.24 and 2.30 Å (Figure 1j,m), respectively. This revealed that the Fe−Fe path contributed to the surrounding coordination environment of Fe centers in Fe−Fe/CN and Fe−Fe/SCN. According to the quantitative EXAFS fitting results for Fe−Fe/CN and Fe−Fe/SCN demonstrated in Tables S8 and S9 and Figures 1k,n, and S10, the average coordination number of the Fe−Fe path was 1.2 and 0.9, respectively, suggesting that a center site of dual Fe atoms (Fe−Fe) dominated in the catalyst structure of Fe−Fe/CN (inset in Figure 1k) and Fe−Fe/SCN (inset in Figure 1n).

Fe−Fe Double-Atom Catalysis for MHV-A59 Disinfection in Diverse Environmental Matrices. To achieve promising disinfection from Fe single-atom and Fe−Fe double-atom catalysis, we first used phenol as a probe compound to investigate the catalytic performance of four different catalysts (i.e., Fe/CN, Fe/SCN, Fe−Fe/CN, and Fe−Fe/SCN) upon PMS activation (Text S9). As shown in Figure S11b,c, regardless of whether catalysts were prepared on the support of CN or SCN, Fe−Fe double-atom catalysts were 3.32−3.50 times more reactive than their counterpart of Fe single-atom catalysts for phenol oxidation by activating PMS. In addition, Fe−Fe/SCN and Fe/SCN degraded phenol 10.4 and 11.0 times faster than Fe−Fe/CN and Fe/CN, respectively (Figure S11c). Notably, all catalysts had a similar Fe loading (0.51 ± 0.09 wt %, Table S6). These results highlighted the excellent performance of catalytic oxidation by introducing the Fe−Fe dimer and the S-dopant into the catalyst, and Fe−Fe/SCN was therefore selected for the following MHV-A59 disinfection tests.

https://doi.org/10.1021/acs.est.3c00163
Environ. Sci. Technol. XXXX, XXX, XXX−XXX

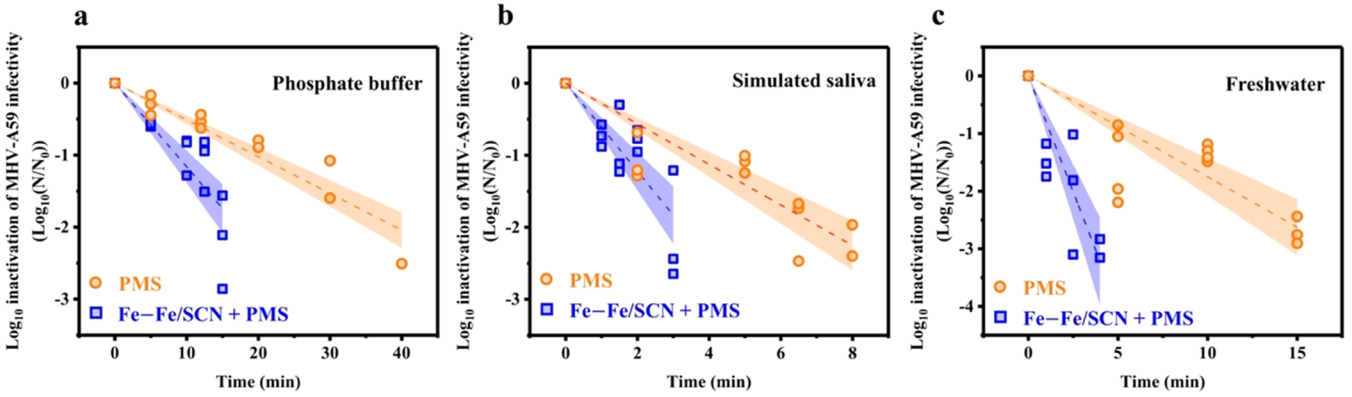

Figure 2. Performance of MHV-A59 disinfection by PMS-alone treatment and Fe−Fe double-atom catalysis. MHV-A59 disinfection by PMS-alone and Fe−Fe/SCN-activated PMS in (a) a phosphate buffer (pH 7, 10 mM), (b) simulated saliva, and (c) freshwater (Potomac River water). Experimental conditions: initial MHV-A59 load before disinfection of ca. 10^7 gene copies well^{-1} in the inoculum, initial MHV-A59 infectivity before disinfection of ca. 10^{10} gene copies well^{-1} as determined by ICC-RT-qPCR, initial PMS concentration of 0.1 mM (for the phosphate buffer and freshwater) and 0.2 mM (for simulated saliva), and catalyst loading of 1.0 g L^{-1}. The inactivation rate constants of MHV-A59 following PMS-alone and Fe−Fe/SCN-activated PMS disinfection in each environmental matrix were statistically different (p <0.05); 95% confidence bands were shown in transparent navy and orange. n = 3−4.

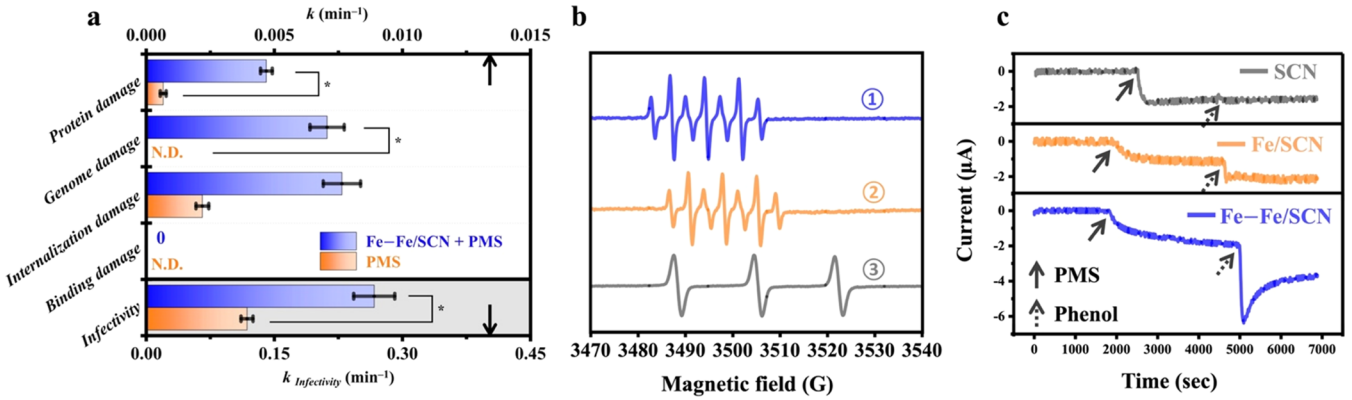

Figure 3. Mechanism of MHV-A59 disinfection and PMS activation by Fe−Fe double-atom catalysis. (a) Damage of MHV-A59 proteins, genomes, binding, internalization, and infectivity by PMS-alone and Fe−Fe/SCN-activated PMS treatments. Total viral protein concentrations during disinfection were quantified by the BCA assay, and protein damage rate constants are calculated from Figure S16. The true damage rate constants of virus binding and internalization are shown. Damage of the viral genome and virus binding to host cells was not detected (N.D.) in PMS-alone disinfection (Figure S27). The observed damage rate constant of virus binding to host cells was not statistically different from the damage rate constant of the viral genome in Fe−Fe/SCN-activated PMS disinfection (Figure S27); therefore, the true damage rate constant of virus binding by Fe−Fe/SCN-activated PMS was assigned to zero. Experimental conditions for virus disinfection and genome, binding, and internalization damage assays: initial MHV-A59 load of ca. 10^7 gene copies well^{-1} in the inoculum, initial MHV-A59 infectivity of ca. 10^{10} gene copies well^{-1} as determined by ICC-RT-qPCR, initial PMS concentration of 0.1 mM, catalyst loading of 1.0 g L^{-1}, and phosphate buffer (pH 7, 10 mM). n = 3. Experimental conditions for the protein damage assay: initial protein concentration of ca. 100 μg of protein mL^{-1}, initial PMS concentration of 0.1 mM, catalyst loading of 1.0 g L^{-1}, and phosphate buffer (pH 7, 10 mM). n = 2. * p < 0.05. (b) EPR spectra of DMPO spin adducts in ① a phosphate buffer and in ② 10% (v/v) ethanol and ③ EPR spectra of TEMP spin adducts in the phosphate buffer for the Fe−Fe/SCN-activated PMS system. Experimental conditions: initial PMS concentration of 1 mM, initial DMPO or TEMP concentration of 60 mM, catalyst loading of 0.2 g L^{-1}, phosphate buffer (pH 7, 10 mM) or 10% (v/v) ethanol, and reaction time of 1 min. (c) Chronoamperometric curves of electron-transfer tests between phenol and PMS on SCN, Fe/SCN, and Fe−Fe/SCN. Arrows illustrate the time when PMS and phenol were injected into the electrochemical cell, respectively.

We then selected a phosphate buffer as a model system and simulated saliva and freshwater as representative environmental matrices, which provided insights into fomite and waterborne transmission of environmental pathogens, to understand the potency of double-atom catalysis for murine coronavirus disinfection. MHV-A59 survived in all three matrices with a negligible infectivity loss with the presence of Fe−Fe/SCN alone but the absence of PMS (Figure S12). The amendment of a PMS dosage of 0.1 mM to Fe−Fe/SCN resulted in rapid inactivation of MHV-A59 in phosphate buffer, with a pseudo-first-order reaction rate constant of 0.267 ± 0.024 min^{-1}, which was 2.26 times higher than that in PMS-alone disinfection with the same PMS dosage (0.118 ± 0.007 min^{-1}, Figure 2a). PMS consumption was also increased in Fe−Fe/SCN-mediated disinfection when compared to PMS-alone disinfection ((3.82 ± 0.36) × 10^{-2} versus (8.75 ± 0.75) × 10^{-3} min^{-1}, Figure S13). CT values were also calculated (Table S10). Interestingly, no apparent MHV-A59 inactivation was observed in Fe−Fe/SCN-activated PMS and PMS-alone treatments in simulated saliva with a PMS concentration of 0.1 mM (Figure S14). Simulated saliva contained proteins (Table S1) that also competed for PMS (Figure S15), lowering the

https://doi.org/10.1021/acs.est.3c00163
Environ. Sci. Technol. XXXX, XXX, XXX−XXX

effectiveness of PMS in disinfection. We increased the PMS dosage to 0.2 mM; hence, Fe−Fe/SCN-activated PMS achieved 2.17 times better performance for MHV-A59 disinfection than PMS-alone treatment (1.41 ± 0.14 versus 0.649 ± 0.046 min^{-1}, Figure 2b). Efficient disinfection of MHV-A59 in freshwater was also realized in the Fe−Fe/SCN-activated PMS system, and 4.60 times faster reaction kinetics was observed when compared to that of the PMS-alone system at 0.1 mM of PMS (1.85 ± 0.20 versus 0.403 ± 0.035 min^{-1}, Figure 2c). Rapid disinfection of MHV-A59 was achieved in all model and environmental matrices with the aid of the Fe−Fe double-atom catalyst, which demonstrates the broad applicability of double-atom catalysts for engineering interventions for environmental pathogen control. Special attention should be paid to the different matrices with diverse compositions and varying concentrations of salts and organics, which could result in potential interactions between metal atoms and anions, virus aggregation, and oxidant consumption and consequently impact the effectiveness of disinfection.

Evaluation of MHV-A59 Protein, Lipid, and Genome Damage following Fe−Fe Double-Atom Catalysis. The survivability of viruses during disinfection treatments is dependent on the susceptibility of essential biomolecules of viral particles, including lipids (for enveloped viruses), proteins, and nucleic acids (genomes).[30,46] Conventional disinfection methods such as chlorination, ozonation, and ultraviolet (UV_{254}) radiation target differently on enveloped viruses, for example, UV_{254} radiation mainly attacks viral genomes, ozone can oxidize viral lipids, and viral proteins are more vulnerable under both free chlorine and ozone treatment.[46,47] Accordingly, to better understand why MHV-A59 gradually lost infectivity during PMS-driven (i.e., PMS-alone and Fe−Fe/SCN-activated PMS) treatments, we measured reactions in proteins, lipids, and genomes of MHV-A59 during inactivation. Murine coronavirus has four major structural proteins: the spike (S) protein, nucleocapsid (N) protein, membrane (M) protein, and the envelope (E) protein; each protein plays a role in retaining virus integrity, and damage to structural proteins could interfere with murine coronavirus lifecycle, resulting in the loss of virus infectivity eventually.[2,48,49] Here, we first monitored the dynamic changes in total viral proteins during PMS-alone and Fe−Fe/SCN-activated PMS treatments. As shown in Figures 3a and S16, total viral protein concentration of MHV-A59 was reduced upon PMS-driven oxidation, and the reduction was more significant for the treatment by Fe−Fe/SCN-activated PMS than PMS alone ($k_{protein\ damage}$ of (4.69 ± 0.23) × 10^{-3} versus (6.61 ± 1.16) × 10^{-4} min^{-1}). To further demonstrate how Fe−Fe double-atom catalysis induced more decay on viral proteins, we measured protein carbonyl, a widely used biomarker to reflect the oxidative damage on proteins,[50] in MHV-A59 after disinfection. As shown in Figure S17, although protein carbonyl was determined after both PMS-alone and Fe−Fe/SCN-activated PMS treatments, the oxidation by Fe−Fe/SCN-activated PMS did not contribute to protein carbonyl formation compared to PMS-alone treatment because a similar protein carbonyl content of MHV-A59 was generated after 90 min of reactions (0.922 ± 0.142 versus 0.986 ± 0.139 nmol of carbonyls per mg of protein, Figure S17). These observations indicated that Fe−Fe/SCN-activated PMS stimulated more oxidative damage on viral proteins compared to PMS-alone treatment, but the consequence of oxidation did not contribute to protein carbonylation. Since the involvement of multiple forms of reactive oxygen species (ROS) (i.e., $^{\bullet}OH$, superoxide anion radical ($O_2^{\bullet-}$), and $^1O_2$) in protein oxidation can result in the addition of carbonyl groups of proteins,[28,51−53] we speculated that ROS might not participate in Fe−Fe/SCN-activated PMS treatment. To clearly demonstrate the reactive species presented in Fe−Fe double-atom catalysis, electron paramagnetic resonance (EPR) spectroscopy in conjunction with 5,5-dimethyl-1-pyrroline-*N*-oxide (DMPO) and 2,2,6,6-tetramethyl-4-piperidinol (TEMP) as trapping agents was first used to illustrate the presence of radicals ($^{\bullet}OH$, sulfate anion radical ($SO_4^{\bullet-}$), and $O_2^{\bullet-}$) and $^1O_2$, respectively (Text S10). As shown in Figures 3b, S18, and S19, EPR spectroscopy did not detect the signal of DMPO-$^{\bullet}OH$, DMPO-$SO_4^{\bullet-}$, or DMPO-$O_2^{\bullet-}$ adducts in the Fe−Fe/SCN-activated PMS system; only the signal of 5,5-dimethylpyrrolidone-(2)-oxyl-(1) (DMPOX) (intensity ratio of 1:2:1:2:1:2:1) was detected, which was originated from the direct oxidation of DMPO.[42] Moreover, EPR spectroscopy revealed the signal of the TEMP-$^1O_2$ adduct (2,2,6,6-tetramethyl-4-piperidinol-*N*-oxyl (TEMPO)) in both PMS-alone and Fe−Fe/SCN-activated PMS systems (Figures 3b and S20).[42] The presence of the TEMPO signal could illustrate the existence of $^1O_2$; however, it did not prove that $^1O_2$ was the dominant reactive species participated in organics transformation. Thus, we then measured the oxidation of furfuryl alcohol (FFA), a probe compound for $^1O_2$, in the Fe−Fe/SCN-activated PMS system.[54] As shown in Figure S21a, FFA decay was clearly observed in PMS treatment alone, which was driven by direct oxidation instead of $^1O_2$ attack,[54] whereas FFA oxidation was significantly inhibited in the Fe−Fe/SCN-activated PMS system. Since the depletion of PMS would suppress FFA oxidation,[54] we further analyzed PMS consumption in PMS−FFA reactions with and without the presence of Fe−Fe/SCN. As shown in Figure S21b, the PMS level maintained well on Fe−Fe/SCN alone, and more PMS was consumed in PMS−FFA mixtures in the absence of Fe−Fe/SCN than that in the presence of the catalyst. Therefore, Fe−Fe double-atom catalysis indeed did not facilitate FFA oxidation. To evaluate the role of $^1O_2$, we carried out phenol−FFA competitive reactions and compared the rate constants of FFA transformation and phenol oxidation by assuming that $^1O_2$ was the key reactive species involved in the Fe−Fe/SCN-activated PMS system (Text S11 and Figure S22). In contrast to FFA, phenol was not directly oxidized by PMS (Figure S11a) under our experimental conditions; therefore, a steady-state concentration of $^1O_2$ of 4.19 × 10^{-10} M would have been achieved in the Fe−Fe/SCN-activated PMS system based on phenol oxidation kinetics if $^1O_2$ was the key player. However, under such situation, the kinetics of FFA transformation would have been 320 times faster than the measured kinetics. Therefore, based on the above characterizations, $^1O_2$ was excluded from reactive species in the Fe−Fe/SCN-activated PMS system under our experimental conditions.

In addition to ROS, oxidation by high-valent Fe−oxo species and catalyst-mediated electron transfer[19,21,22,42] are two other possible pathways in the Fe−Fe/SCN-activated PMS system. To evaluate the presence of high-valent Fe−oxo species based on their unique oxygen-atom-transfer reaction,[17,42] we introduced phenyl methyl sulfoxide (PMSO) into PMS-alone and Fe−Fe/SCN-activated PMS systems. Phenyl methyl sulfone ($PMSO_2$) was the only oxidation product of PMSO in both treatments (Figure S23a,b), but PMSO oxidation kinetics was not enhanced with the presence of the Fe−Fe

https://doi.org/10.1021/acs.est.3c00163
Environ. Sci. Technol. XXXX, XXX, XXX−XXX

double-atom catalyst (Figure S23c). Therefore, high-valent Fe−oxo species might not play a dominant role in the Fe−Fe/SCN-activated PMS system. We then used the electrochemical analysis to investigate the mechanism of catalyst-mediated electron transfer in the Fe−Fe/SCN-activated PMS system (Text S12). Chronoamperometry was applied to monitor electron transfer from phenol (an electron−donor probe) to PMS[22] with the presence of Fe−Fe/SCN, Fe/SCN, and a reference sample (i.e., SCN), and a negative current flow was detected on electrodes loaded with SCN, Fe/SCN, and Fe−Fe/SCN when PMS was amended (Figure 3c). It is reasonable to speculate that introducing PMS into an unbuffered electrolyte influenced the electrode surface charge or PMS interacted with SCN-based materials. Subsequently, upon the injection of the electron−donor probe, the current immediately increased on Fe/SCN and Fe−Fe/SCN electrodes but not the SCN electrode (Figure 3c). A more significant current increase was observed on the Fe−Fe/SCN electrode than that on the Fe/SCN electrode. The result demonstrated that both Fe single-atom and Fe−Fe double-atom catalysts boosted electrons transferring to PMS, and Fe−Fe/SCN was more reactive. Electrochemical impedance spectroscopy was also used to evaluate the electrochemical properties of catalysts,[22] and SCN, Fe/SCN, and Fe−Fe/SCN all showed similar resistance, illustrating that introducing Fe atoms to the SCN support did not affect the electrochemical impedance of materials (Figure S24). Based on the characterization of reactive species involved in the Fe−Fe/SCN-activated PMS system as abovementioned, Fe−Fe double-atom catalysis was believed to promote catalyst-mediated electron transfer rather than to facilitate the generation of $^{\bullet}OH$, $SO_4^{\bullet-}$, $O_2^{\bullet-}$, $^1O_2$, and high-valent Fe−oxo species in comparison with PMS-alone treatment.

Lipids are also important to determine the stability of the coronavirus envelope, structural integrity, and infectivity. However, MDA adduct formation was not observed upon oxidation by both Fe−Fe/SCN-activated PMS and PMS alone, highlighting that lipids are much less reactive in PMS-driven oxidation (Figure S25). Notably, like protein carbonyls, MDA adducts could also be found under ROS attack.[51,55,56] Moreover, negligible lipid peroxidation also excluded the likelihood of the reaction of amino acid residues (i.e., cysteine, histidine, and lysine) with reactive aldehydes (byproducts of lipid peroxidation), which could contribute to protein carbonyl formation.[50] Last but not least, we quantified viral genome damage because it is another determinant of viral infectivity loss in disinfection since it impedes virus replication. No obvious MHV-A59 genome damage was observed in PMS-alone oxidation, but the presence of Fe−Fe/SCN promoted the genome damage kinetics significantly ($(7.06 \pm 0.67) \times 10^{-3}$ min^{-1}, Figure 3a).

Evaluation of MHV-A59 Binding to and Internalization into Host Cells Following Fe−Fe Double-Atom Catalysis. Coronaviruses need to successfully bind to the receptors expressed on host cells (① in Figure 4a) and subsequently internalize into the host cells (② in Figure 4a) before replication and producing viral progeny (③ in Figure 4a).[2,57] Any damage to virus lifecycle could compromise the infectivity of viruses.[30,48,58] Our results demonstrated that MHV-A59 binding to host cells remained intact after disinfection by PMS-alone and Fe−Fe/SCN-activated PMS, whereas internalization into the host cells was compromised in both treatments, and it was more significantly damaged by Fe−

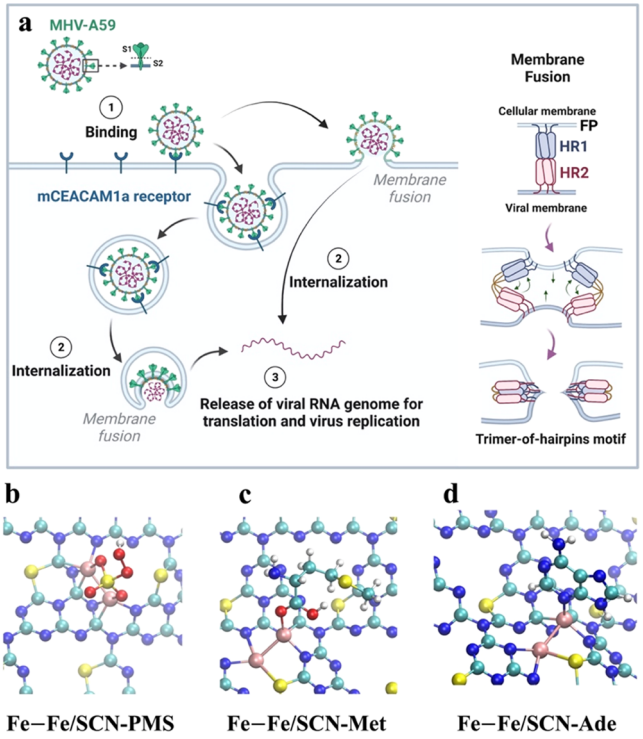

Figure 4. Molecular simulation of MHV-A59 integrity and functionality compromised by Fe−Fe double-atom catalysis. (a) MHV-A59 lifecycle in host cells. Details of membrane fusion between the cellular membrane and the viral membrane are highlighted on the right. Fusion peptide (FP) and the interaction of two heptad repeat regions (HR1 and HR2) are important for membrane fusion. Optimized structure of (b) Fe−Fe/SCN−PMS, (c) Fe−Fe/SCN−Met, and (d) Fe−Fe/SCN−Ade adducts. The carbon, nitrogen, sulfur, oxygen, and iron atoms were depicted in teal, navy, yellow, red, and rose, respectively.

Fe double-atom catalysis ($k_{internalization}$ of $(7.64 \pm 0.73) \times 10^{-3}$ versus $(2.19 \pm 0.25) \times 10^{-3}$ min^{-1}, Figure 3a). The S protein of MHV-A59 is a type I fusion protein that is responsible for mediating both virus binding and internalization.[59] The S protein of MHV-A59 is posttranslationally cleaved into an S1 receptor binding unit and an S2 membrane fusion unit with distinct functions (Table S11).[60] The N-terminal domain (NTD) within the S1 unit recognizes the cell receptor of murine carcinoembryonic antigen-related cell adhesion molecule 1a (mCEACAM1a),[61] and this interaction is critical to determine viral infectivity.[61,62] Particularly, several amino acid residues in NTD of MHV-A59 (highlighted in red in Table S11) are important because they are responsible for the direct contact between the virus and its cell receptor. Interestingly, the reactivity between these amino acids and PMS is low because PMS only reacts with sulfur-containing cysteine and methionine (Met) rapidly, and the reaction rate constant of Met−PMS is 3−6 orders of magnitude higher than those of other amino acids (Table S12).[63,64] In addition, Fe−Fe/SCN-activated PMS likely promoted catalyst-mediated electron transfer in which PMS directly abstracted electrons from organics mediated on Fe−Fe/SCN.[21,22] Therefore, it is reasonable not to see the apparent damage of virus binding after the oxidation by PMS-alone and Fe−Fe/SCN-activated PMS. After binding to the receptor, the putative fusion peptide (FP) and two heptad repeat regions (HR1 and HR2) in the S2 unit play a key role in coronavirus−cell membrane fusion.[65,66]

https://doi.org/10.1021/acs.est.3c00163
Environ. Sci. Technol. XXXX, XXX, XXX−XXX

In membrane fusion, FP is first inserted into the cell membrane, HR2 then binds to HR1 in an antiparallel manner to form a stable six-helix bundle, and the trimer-of-hairpins conformation brings both viral and cell membranes into close proximity (Figure 4a).[66] Several critical amino acid residues in HR1 and HR2 (highlighted in green and magenta in Table S11) contribute to this important HR1/HR2 interaction that facilitates the juxtaposition of viral and cell membranes.[65] Met is one critical hydrophobic residue in HR2, and it is also observed in FP (Table S11); the rapid oxidation of Met by PMS regardless of the presence of the catalyst could explain the significant damage to MHV-A59 internalization found in our study.

Computational Simulations for Understanding MHV-A59 Disinfection by Fe−Fe Double-Atom Catalysis. Experimental results have demonstrated that Fe−Fe double-atom catalysis prompted oxidative damage of viral proteins and genomes and consequently impaired virus lifecycle. To elucidate the mechanism, we used computational simulations to investigate PMS activation on Fe−Fe/SCN and the oxidation of representative amino acids and a representative nucleobase, including Met, tyrosine (Tyr), lysine (Lys), and adenine (Ade). Met is a critical amino acid responsible for MHV-A59 internalization and the most vulnerable amino acid under PMS oxidation; Tyr and Lys are also ubiquitous amino acids in coronavirus proteins and important for viral functions, but they are less susceptible toward PMS oxidation (Tables S11 and S12); Ade was chosen as a typical nucleobase to underscore virus genome damage. First, our simulation results showed that PMS only had a weak physical adsorption onto SCN (i.e., catalyst support without Fe doping) with a small adsorption energy of −4.2 kcal mol^{-1} (Figure S26a), while Fe atoms intercalated in SCN significantly facilitated PMS decomposition through the electron transfer from Fe^{II} to PMS (Figure S26b,c). The direct dissociation of PMS into nonradical species on Fe/SCN featured a large energy drop of −45.6 kcal mol^{-1} (Figure S26b), and Fe−Fe double-atom sites on Fe−Fe/SCN further enlarged it to −157.6 kcal mol^{-1} (Figures 4b and S26c). Our calculations also found that PMS decomposition energy changed from 9.9 to −27.3 kcal mol^{-1} after Fe−Fe double-atom sites were anchored on the SCN substrate, suggesting that Fe−Fe double-atom sites turned PMS decomposition from an endothermic process into an exothermic one, greatly facilitating PMS activation.

For any chemical reaction catalyzed by a substrate, its binding energy (ΔE^b) to the reactant is an important property that governs the formation propensity of a substrate/reactant adduct, which is defined as $\Delta E^b = E_{substrate/reactant} - E_{substrate} - E_{reactant}$, where $E_{substrate/reactant}$, $E_{substrate}$, and $E_{reactant}$ represent energy of the substrate−reactant complex, substrate, and reactant, respectively. As shown in Table S13, ΔE^b of SCN with Met was low at −2.5 kcal mol^{-1} because both SCN and Met are hydrophobic, making their coupling primarily driven by the weak van der Waals interaction, while ΔE^b of Fe−Fe/SCN with Met surged to −113.4 kcal mol^{-1} due to the polarization of SCN through Fe−Fe double-atom site addition. As a result, the coupling between Fe−Fe/SCN and Met was predominantly promoted by the pronounced electrostatic attraction (Figure 4c). Similarly, a large increase of ΔE^b from −3.4 to −125.6 kcal mol^{-1} was also observed on the hydrophobic Ade when SCN was replaced by Fe−Fe/SCN (Table S13 and Figure 4d). For the hydrophilic Tyr and Lys, only moderate increases in ΔE^b were found owing to the already strong electrostatic attraction with the SCN substrate. According to Fermi's golden rule,[67] the electron transfer rate is proportional to the square of the electronic coupling strength. A strong binding generally leads to a strong electronic coupling as the former partially arises from the latter. This prominent correlation between ΔE^b and the electronic coupling strength was evident in Table S13. For instance, the electronic coupling strength of the loosely bound SCN with Met was 1.0 kcal mol^{-1}, which was an order of magnitude smaller than that of the tightly bound Fe−Fe/SCN with Met. On the other hand, a small increase of ΔE^b from −63.8 to −88.4 kcal mol^{-1} for Tyr resulted in a trivial boost of the electronic coupling strength from 3.7 to 4.6 kcal mol^{-1}. Nevertheless, the introduction of Fe−Fe double-atom sites generally strengthened the substrate and reactant binding and intensified their electronic coupling, presumably resulting in faster oxidation of amino acids and the nucleobase. A more direct indicator of this enhanced oxidation was the shift of a reactant's oxidation energy ($\Delta\Delta E^{ox}$) in water upon the presence of Fe−Fe/SCN, which is depicted as $\Delta\Delta E^{ox} = E_{substrate} + E_{reactant} - E_{substrate/reactant} - E_{e^-}$, where E_{e^-} of −35.5 kcal mol^{-1} is the electron's absolute solvation energy in water at 298 K.[68] As shown in Table S14, all of our reactants of interest exhibited notably negative values of $\Delta\Delta E^{ox}$, which ranged from −3.6 to −7.1 kcal mol^{-1}, again illustrating the advanced oxidation via chemically active Fe−Fe double-atom sites intercalated in the SCN backbone. All of these computational results provide first insights that Fe−Fe/SCN facilitates PMS activation and the oxidation of MHV-A59 proteins and genomes, which could in turn compromise virus infectivity.

■ ENVIRONMENTAL IMPLICATIONS

Disinfection, sanitation, and hygiene practices are important engineering interventions to prevent the spread of infectious diseases. To improve disinfection potency, we developed Fe−Fe double-atom catalysts from earth-abundant elements to activate PMS via proposed catalyst-mediated electron-transfer mechanism, which enabled rapid murine coronavirus inactivation. We applied both wet-lab techniques and computational simulations to investigate how Fe−Fe double-atom sites facilitated PMS activation and advanced virus inactivation. However, special attention should be paid to some potential caveats. First, the RT-qPCR approach used in this study determining the damage to virus genomes, binding, and internalization only quantified limited bases in the viral genome, and a genome-wide approach should be considered in future studies since longer amplicons can improve the sensitivity of RT-qPCR.[30] Next, our simulations focused on the oxidation of amino acids and a nucleobase instead of proteins/peptides and genomes, and future studies can integrate mass spectrometry with simulations directly targeting polypeptide and polynucleotide chains to specifically highlight oxidative damage, though simulation costs should be considered for running larger molecules. In addition, our study also revealed that the damage of virus binding and internalization did not fully capture the loss of viral infectivity after disinfection (Table S15). Therefore, it is necessary to identify the vulnerability of each step in the virus lifecycle toward disinfection treatments in the future, and the pathogen-oriented delivery of disinfectants targeting the susceptible biofunctions of pathogens will render benefits to advance disinfection.

https://doi.org/10.1021/acs.est.3c00163
Environ. Sci. Technol. XXXX, XXX, XXX−XXX

Our study, as a proof of concept, demonstrates for the first time that double-atom catalysis holds promise for environmental pathogen control. When applying heterogeneous catalysts for practical engineering applications, incidental release of the catalysts may pose negative impacts on aquatic lives and human health. Therefore, in water treatment, continuous flow reactors with microfiltration membranes employed to separate the catalysts or with packed columns that immobilize catalysts within the reactor will largely reduce catalyst leaching and minimize secondary pollution. Another challenge in implementing this catalyst in practice is the low metal loading and the consequent high catalyst dosage for reactions, for example, a high catalyst loading of 1.0 g L^{-1} was applied in our study for achieving desired disinfection performance because of the low Fe loading (0.45 wt %) on Fe−Fe/SCN. Based on the CT value for virus disinfection, Fe−Fe/SCN-activated PMS treatment outperformed chloramination, but it was inferior to the treatment by chlorine, chlorine dioxide, and ozone (Table S10). Fortunately, recent advancements have shown that up to about 20 wt % of transition metals were atomically dispersed and loaded onto catalysts without aggregation,[69] therefore, future studies should focus on developing double-atom catalysts with an increased metal loading, which in turn reduces the cost and material and energy footprint for catalyst fabrication and advances the disinfection potency to achieve eco-friendly and robust disinfection for protecting the public health.

■ ASSOCIATED CONTENT

Supporting Information

The Supporting Information is available free of charge at https://pubs.acs.org/doi/10.1021/acs.est.3c00163.

Details of all chemicals and reagents; catalyst synthesis; TEM and STEM images of Fe−Fe/SCN; statistical analysis on projected Fe−Fe distance from AC-HAADF-STEM characterization of Fe−Fe/CN and Fe−Fe/SCN; XRD pattern, ATR-FTIR spectra, nitrogen adsorption−desorption isotherm, basic physical and chemical properties of catalysts and reference samples; XPS spectra of Fe−Fe/CN, Fe−Fe/SCN, and SCN; normalized XANES spectra and the FT k^3-weighted EXAFS spectra at Fe *K*-edge of Fe/CN and Fe/SCN; EXAFS data fitting results in *k*-space and fitted structures of Fe−Fe/CN and Fe−Fe/SCN; PMS quantification; electrochemical analysis and impedance spectrum of Fe/SCN, Fe−Fe/SCN, and SCN; HPLC analysis parameters; phenol adsorption and oxidation on catalysts; characterizations of $^{\bullet}OH$, $SO_4^{\bullet-}$, $O_2^{\bullet-}$, $^1O_2$, and high-valent Fe−oxo species, including EPR analysis of DMPO and TEMP spin adducts, FFA oxidation in PMS-alone and Fe−Fe/SCN-activated PMS systems, PMS consumption in PMS−FFA reactions with and without the presence of the Fe−Fe/SCN catalyst, and evaluation of PMSO-to-$PMSO_2$ conversion kinetics; L-929 cells culturing and MHV-A59 propagation; MHV-A59 infectivity, binding, and internalization assays; sequence information used in RT-qPCR for MHV-A59 quantification; qPCR inhibition test; linear correlation of the infectivity of MHV-A59 (quenched by $Na_2S_2O_3$) with the viral load before infection; PMS consumption during MHV-A59 inactivation following PMS-alone and Fe−Fe/SCN-activated PMS treatments; CT values for MHV-A59 inactivation by PMS-alone and Fe−Fe/SCN-activated PMS treatments; resistance of MHV-A59 to PMS and the depletion of PMS in simulated saliva matrix; particle size distribution and concentration of purified MHV-A59 samples; linear correlation of total viral protein concentration in purified MHV-A59 samples quantified by the Pierce BCA protein assay with the viral load; characterizations of MHV-A59 genome damage, protein (total viral protein and protein carbonyl levels) and lipid oxidation, and observed damage to MHV-A59 lifecycle during PMS-alone and Fe−Fe/SCN-activated PMS treatments; evaluation of Fe−Fe/SCN for oxidizing amino acids and a nucleobase by computational simulations; compositions of simulated saliva and water quality parameters of the Potomac River; amino acid sequences and critical residues in MHV-A59 spike protein; reactivity and selectivity of PMS toward amino acids; and additional references (PDF)

■ AUTHOR INFORMATION

Corresponding Authors

David P. Durkin − *Department of Chemistry, United States Naval Academy, Annapolis, Maryland 21402, United States;* orcid.org/0000-0001-5979-8449; Phone: 410-293-6601.; Email: durkin@usna.edu; Fax: 410−293−2218

Hanning Chen − *Texas Advanced Computing Center, The University of Texas at Austin, Austin, Texas 78758, United States;* orcid.org/0000-0003-3568-8039; Phone: 512-475-9411; Email: hanning.chen@austin.utexas.edu; Fax: 512-475-9445

Danmeng Shuai − *Department of Civil and Environmental Engineering, The George Washington University, Washington, District of Columbia 20052, United States;* orcid.org/0000-0003-3817-4092; Phone: 202-994-0506.; Email: danmengshuai@gwu.edu; Fax: 202-994-0127; http://materwatersus.weebly.com/

Authors

Zhe Zhou − *Department of Civil and Environmental Engineering, The George Washington University, Washington, District of Columbia 20052, United States;* orcid.org/0000-0003-3253-6355

Mengqiao Li − *Department of Civil and Environmental Engineering, The George Washington University, Washington, District of Columbia 20052, United States;* orcid.org/0000-0002-0567-9716

Yuxin Zhang − *Department of Chemistry, Virginia Tech, Blacksburg, Virginia 24061, United States;* orcid.org/0000-0002-2830-4159

Lingchen Kong − *Department of Civil and Environmental Engineering, The George Washington University, Washington, District of Columbia 20052, United States*

Virginia F. Smith − *Department of Chemistry, United States Naval Academy, Annapolis, Maryland 21402, United States;* orcid.org/0000-0003-2178-5823

Mengyang Zhang − *Department of Civil and Environmental Engineering, The George Washington University, Washington, District of Columbia 20052, United States*

Anders J. Gulbrandson − *Department of Chemistry, United States Naval Academy, Annapolis, Maryland 21402, United States*

https://doi.org/10.1021/acs.est.3c00163
Environ. Sci. Technol. XXXX, XXX, XXX−XXX

Gordon H. Waller − *Chemistry Division, United States Naval Research Laboratory, Washington, District of Columbia 20375, United States*

Feng Lin − *Department of Chemistry, Virginia Tech, Blacksburg, Virginia 24061, United States;* orcid.org/0000-0002-3729-3148

Xitong Liu − *Department of Civil and Environmental Engineering, The George Washington University, Washington, District of Columbia 20052, United States;* orcid.org/0000-0002-5197-3422

Complete contact information is available at: https://pubs.acs.org/10.1021/acs.est.3c00163

Notes

The authors declare no competing financial interest.

■ ACKNOWLEDGMENTS

We acknowledge the National Science Foundation grant (CBET-1932820) and United States Department of Agriculture−National Institute of Food and Agriculture grant (2022-67022-36696) for supporting our research. We also acknowledge the financial support from the Air Force Office of Scientific Research (MIPR# F4FGA02032G001), the support from the start-up funds received from the Department of Civil and Environmental Engineering at The George Washington University, and the financial support from the Office of Naval Research. We thank the United States Naval Academy for material characterization (XRD, ATR-FTIR, and Brunauer−Emmett−Teller (BET) nitrogen adsorption−desorption analysis) and EPR analysis, the Carderock Division of the Naval Surface Warfare Center for XPS analysis, the Argonne National Laboratory for XAS analysis, The George Washington University Nanofabrication and Imaging Center for TEM analysis, the Microanalysis Laboratory at the University of Illinois at Urbana-Champaign for ICP-OES analysis, and Loudoun Water (VA) for providing the freshwater sample. We also thank Dr. Nihal Altan-Bonnet from the National Heart Lung and Blood Institute at the National Institutes of Health for providing MHV-A59 and NanoSight access. Any opinions, findings and conclusions, or recommendations expressed in this study are those of the authors and do not reflect the views of the U.S. Air Force or the U.S. Navy.

■ REFERENCES

(1) Zimmer, S. M.; Burke, D. S. Historical perspective — emergence of influenza A (H1N1) viruses. *N. Engl. J. Med.* **2009**, *361*, 279−285.

(2) Jackson, C. B.; Farzan, M.; Chen, B.; Choe, H. Mechanisms of SARS-CoV-2 entry into cells. *Nat. Rev. Mol. Cell Biol.* **2022**, *23*, 3−20.

(3) Cohen, J. Monkeypox outbreak questions intensify as cases soar. *Science* **2022**, *376*, 902−903.

(4) Bushman, F. D.; McCormick, K.; Sherrill-Mix, S. Virus structures constrain transmission modes. *Nat. Microbiol.* **2019**, *4*, 1778−1780.

(5) van Doremalen, N.; Bushmaker, T.; Morris, D. H.; Holbrook, M. G.; Gamble, A.; Williamson, B. N.; Tamin, A.; Harcourt, J. L.; Thornburg, N. J.; Gerber, S. I.; Lloyd-Smith, J. O.; de Wit, E.; Munster, V. J. Aerosol and surface stability of SARS-CoV-2 as compared with SARS-CoV-1. *N. Engl. J. Med.* **2020**, *382*, 1564−1567.

(6) Silverman, A. I.; Boehm, A. B. Systematic review and meta-analysis of the persistence of enveloped viruses in environmental waters and wastewater in the absence of disinfectants. *Environ. Sci. Technol.* **2021**, *55*, 14480−14493.

(7) Edwards, C. E.; Yount, B. L.; Graham, R. L.; Leist, S. R.; Hou, Y. X. J.; Dinnon, K. H.; Sims, A. C.; Swanstrom, J.; Gully, K.; Scobey, T. D.; Cooley, M. R.; Currie, C. G.; Randell, S. H.; Baric, R. S. Swine acute diarrhea syndrome coronavirus replication in primary human cells reveals potential susceptibility to infection. *Proc. Natl. Acad. Sci. U.S.A.* **2020**, *117*, 26915−26925.

(8) Grange, Z. L.; Goldstein, T.; Johnson, C. K.; Anthony, S.; Gilardi, K.; Daszak, P.; Olival, K. J.; O'Rourke, T.; Murray, S.; Olson, S. H.; Togami, E.; Vidal, G.; Panel, E.; Mazet, J. A. K.; Consortium, P.; et al. Ranking the risk of animal-to-human spillover for newly discovered viruses. *Proc. Natl. Acad. Sci. U.S.A.* **2021**, *118*, e2002324118.

(9) Rohani, P.; Breban, R.; Stallknecht, D. E.; Drake, J. M. Environmental transmission of low pathogenicity avian influenza viruses and its implications for pathogen invasion. *Proc. Natl. Acad. Sci. U.S.A.* **2009**, *106*, 10365−10369.

(10) Bogler, A.; Packman, A.; Furman, A.; Gross, A.; Kushmaro, A.; Ronen, A.; Dagot, C.; Hill, C.; Vaizel-Ohayon, D.; Morgenroth, E.; Bertuzzo, E.; Wells, G.; Kiperwas, H. R.; Horn, H.; Negev, I.; Zucker, I.; Bar-Or, I.; Moran-Gilad, J.; Balcazar, J. L.; Bibby, K.; Elimelech, M.; Weisbrod, N.; Nir, O.; Sued, O.; Gillor, O.; Alvarez, P. J.; Crameri, S.; Arnon, S.; Walker, S.; Yaron, S.; Nguyen, T. H.; Berchenko, Y.; Hu, Y. X.; Ronen, Z.; Bar-Zeev, E. Rethinking wastewater risks and monitoring in light of the COVID-19 pandemic. *Nat. Sustainable* **2020**, *3*, 981−990.

(11) Dewey, H. M.; Jones, J. M.; Keating, M. R.; Budhathoki-Uprety, J. Increased use of disinfectants during the COVID-19 pandemic and its potential impacts on health and safety. *ACS Chem. Health Saf.* **2022**, *29*, 27−38.

(12) Tulalamba, W.; Assawamakin, A.; Thayananuphat, A.; Viprakasit, V. Evaluation of potassium peroxymonosulfate (MPS) efficacy against SARS-CoV-2 virus using RT-qPCR-based method. *Int. J. Infect. Dis.* **2021**, *110*, 162−164.

(13) Ragazzo, P.; Chiucchini, N.; Piccolo, V.; Spadolini, M.; Carrer, S.; Zanon, F.; Gehr, R. Wastewater disinfection: long-term laboratory and full-scale studies on performic acid in comparison with peracetic acid and chlorine. *Water Res.* **2020**, *184*, 116169.

(14) Borgmann-Strahsen, R. Comparative assessment of different biocides in swimming pool water. *Int. Biodeterior. Biodegradation* **2003**, *51*, 291−297.

(15) Hashizume, M.; Aoki, K.; Ohno, S.; Kitaichi, N.; Yawata, N.; Gonzalez, G.; Nonaka, H.; Sato, S.; Takaoka, A. Disinfectant potential in inactivation of epidemic keratoconjunctivitis-related adenoviruses by potassium peroxymonosulfate. *Eur. J. Ophthalmol.* **2021**, *31*, 379−384.

(16) Wu, Q. Y.; Wang, J.; Wang, Z. W.; Xu, Y. L.; Xing, Z. H.; Zhang, X. Y.; Guan, Y. T.; Liao, G. F.; Li, X. Z. High-loaded single Cu atoms decorated on N-doped graphene for boosting Fenton-like catalysis under neutral pH. *J. Mater. Chem. A* **2020**, *8*, 13685−13693.

(17) Zhang, L. S.; Jiang, X. H.; Zhong, Z. A.; Tian, L.; Sun, Q.; Cui, Y. T.; Lu, X.; Zou, J. P.; Luo, S. L. Carbon nitride supported high-loading Fe single-atom catalyst for activating of peroxymonosulfate to generate $^1O_2$ with 100% selectivity. *Angew. Chem., Int. Ed.* **2021**, *60*, 21751−21755.

(18) Xiong, Y.; Li, H. C.; Liu, C. W.; Zheng, L. R.; Liu, C.; Wang, J. O.; Liu, S. J.; Han, Y. H.; Gu, L.; Qian, J. S.; Wang, D. S. Single-atom Fe catalysts for Fenton-like reactions: roles of different N species. *Adv. Mater.* **2022**, *34*, 2110653.

(19) Zhou, X.; Ke, M. K.; Huang, G. X.; Chen, C.; Chen, W. X.; Liang, K.; Qu, Y. T.; Yang, J.; Wang, Y.; Li, F. T.; Yu, H. Q.; Wu, Y. E. Identification of Fenton-like active Cu sites by heteroatom modulation of electronic density. *Proc. Natl. Acad. Sci. U.S.A.* **2022**, *119* (8), e2119492119.

(20) Zhang, Y. J.; Huang, G. X.; Winter, L. R.; Chen, J. J.; Tian, L. L.; Mei, S. C.; Zhang, Z.; Chen, F.; Guo, Z. Y.; Ji, R.; You, Y. Z.; Li, W. W.; Liu, X. W.; Yu, H. Q.; Elimelech, M. Simultaneous nanocatalytic surface activation of pollutants and oxidants for highly efficient water decontamination. *Nat. Commun.* **2022**, *13*, No. 3005.

(21) Lee, J.; von Gunten, U.; Kim, J. H. Persulfate-based advanced oxidation: critical assessment of opportunities and roadblocks. *Environ. Sci. Technol.* **2020**, *54*, 3064−3081.

(22) Ren, W.; Cheng, C.; Shao, P. H.; Luo, X. B.; Zhang, H.; Wang, S. B.; Duan, X. G. Origins of electron-transfer regime in persulfate-based nonradical oxidation processes. *Environ. Sci. Technol.* **2022**, *56*, 78−97.
(23) Ying, Y. R.; Luo, X.; Qiao, J. L.; Huang, H. T. ″More is different:″ synergistic effect and structural engineering in double-atom catalysts. *Adv. Funct. Mater.* **2021**, *31*, 2007423.
(24) Zhang, J. Q.; Zhao, Y. F.; Chen, C.; Huang, Y. C.; Dong, C. L.; Chen, C. J.; Liu, R. S.; Wang, C. Y.; Yan, K.; Li, Y. D.; Wang, G. X. Tuning the coordination environment in single-atom catalysts to achieve highly efficient oxygen reduction reactions. *J. Am. Chem. Soc.* **2019**, *141*, 20118−20126.
(25) Standard test method for evaluation of effectiveness of decontamination procedures for air-permeable materials when challenged with biological aerosols containing human pathogenic viruses. *ASTM Int.* 2011, (Designation: E2720-10).
(26) Larivé, O.; Brandani, J.; Dubey, M.; Kohn, T. An integrated cell culture reverse transcriptase quantitative PCR (ICC-RTqPCR) method to simultaneously quantify the infectious concentrations of eight environmentally relevant enterovirus serotypes. *J. Virol. Methods* **2021**, *296*, 114225.
(27) Bustin, S. A.; Benes, V.; Garson, J. A.; Hellemans, J.; Huggett, J.; Kubista, M.; Mueller, R.; Nolan, T.; Pfaffl, M. W.; Shipley, G. L.; Vandesompele, J.; Wittwer, C. T. The MIQE guidelines: minimum information for publication of Quantitative Real-Time PCR experiments. *Clin. Chem.* **2009**, *55*, 611−622.
(28) Sun, H. W.; Li, G. Y.; Nie, X.; Shi, H. X.; Wong, P. K.; Zhao, H. J.; An, T. C. Systematic approach to in-depth understanding of photoelectrocatalytic bacterial inactivation mechanisms by tracking the decomposed building blocks. *Environ. Sci. Technol.* **2014**, *48*, 9412−9419.
(29) Tai, C. J.; Li, C. L.; Tai, C. J.; Wang, C. K.; Lin, L. T. Early viral entry assays for the identification and evaluation of antiviral compounds. *J. Vis. Exp.* **2015**, *104*, e53124.
(30) Wigginton, K. R.; Pecson, B. M.; Sigstam, T.; Bosshard, F.; Kohn, T. Virus inactivation mechanisms: impact of disinfectants on virus function and structural integrity. *Environ. Sci. Technol.* **2012**, *46*, 12069−12078.
(31) Kühne, T. D.; Iannuzzi, M.; Del Ben, M.; Rybkin, V. V.; Seewald, P.; Stein, F.; Laino, T.; Khaliullin, R. Z.; Schütt, O.; Schiffmann, F.; Golze, D.; Wilhelm, J.; Chulkov, S.; Bani-Hashemian, M. H.; Weber, V.; Borštnik, U.; Taillefumier, M.; Jakobovits, A. S.; Lazzaro, A.; Pabst, H.; Müller, T.; Schade, R.; Guidon, M.; Andermatt, S.; Holmberg, N.; Schenter, G. K.; Hehn, A.; Bussy, A.; Belleflamme, F.; Tabacchi, G.; Glöß, A.; Lass, M.; Bethune, I.; Mundy, C. J.; Plessl, C.; Watkins, M.; VandeVondele, J.; Krack, M.; Hutter, J. CP2K: an electronic structure and molecular dynamics software package — Quickstep: efficient and accurate electronic structure calculations. *J. Chem. Phys.* **2020**, *152*, 194103.
(32) Heyd, J.; Scuseria, G. E.; Ernzerhof, M. Erratum: "Hybrid functionals based on a screened Coulomb potential" [J. Chem. Phys. 118, 8207 (2003)]. *J. Chem. Phys.* **2006**, *124*, 219906.
(33) Goedecker, S.; Teter, M.; Hutter, J. Separable dual-space Gaussian pseudopotentials. *Phys. Rev. B* **1996**, *54*, 1703−1710.
(34) Dunning, T. H. Gaussian basis sets for use in correlated molecular calculations. I. The atoms boron through neon and hydrogen. *J. Chem. Phys.* **1989**, *90*, 1007−1023.
(35) Bani-Hashemian, M. H.; Brück, S.; Luisier, M.; VandeVondele, J. A generalized Poisson solver for first-principles device simulations. *J. Chem. Phys.* **2016**, *144*, 044113.
(36) Wu, Q.; Van Voorhis, T. Constrained density functional theory and its application in long-range electron transfer. *J. Chem. Theory Comput.* **2006**, *2*, 765−774.
(37) Farazdel, A.; Dupuis, M.; Clementi, E.; Aviram, A. Electric-field induced intramolecular electron transfer in spiro.pi.-electron systems and their suitability as molecular electronic devices. A theoretical study. *J. Am. Chem. Soc.* **1990**, *112*, 4206−4214.
(38) Blöchl, P. E. Electrostatic decoupling of periodic images of plane-wave-expanded densities and derived atomic point charges. *J. Chem. Phys.* **1995**, *103*, 7422−7428.
(39) Broyden, C. G. The convergence of a class of double-rank minimization algorithms 1. general considerations. *IMA J. Appl. Math.* **1970**, *6*, 76−90.
(40) Pulay, P. Convergence acceleration of iterative sequences. the case of scf iteration. *Chem. Phys. Lett.* **1980**, *73*, 393−398.
(41) VandeVondele, J.; Hutter, J. An efficient orbital transformation method for electronic structure calculations. *J. Chem. Phys.* **2003**, *118*, 4365−4369.
(42) Li, H. C.; Shan, C.; Pan, B. C. Fe(III)-doped g-C_3N_4 mediated peroxymonosulfate activation for selective degradation of phenolic compounds via high-valent iron-oxo species. *Environ. Sci. Technol.* **2018**, *52*, 2197−2205.
(43) Tian, S. B.; Fu, Q.; Chen, W. X.; Feng, Q. C.; Chen, Z.; Zhang, J.; Cheong, W. C.; Yu, R.; Gu, L.; Dong, J. C.; Luo, J.; Chen, C.; Peng, Q.; Draxl, C.; Wang, D. S.; Li, Y. D. Carbon nitride supported Fe2 cluster catalysts with superior performance for alkene epoxidation. *Nat. Commun.* **2018**, *9*, 3181.
(44) Shalom, M.; Inal, S.; Fettkenhauer, C.; Neher, D.; Antonietti, M. Improving carbon nitride photocatalysis by supramolecular preorganization of monomers. *J. Am. Chem. Soc.* **2013**, *135*, 7118−7121.
(45) Tian, S. B.; Wang, B. X.; Gong, W. B.; He, Z. Z.; Xu, Q.; Chen, W. X.; Zhang, Q. H.; Zhu, Y. Q.; Yang, J. R.; Fu, Q.; Chen, C.; Bu, Y. X.; Gu, L.; Sun, X. M.; Zhao, H. J.; Wang, D. S.; Li, Y. D. Dual-atom Pt heterogeneous catalyst with excellent catalytic performances for the selective hydrogenation and epoxidation. *Nat. Commun.* **2021**, *12*, 3181.
(46) Ye, Y. Y.; Chang, P. H.; Hartert, J.; Wigginton, K. R. Reactivity of enveloped virus genome, proteins, and lipids with free chlorine and UV_{254}. *Environ. Sci. Technol.* **2018**, *52*, 7698−7708.
(47) Manjunath, S. N.; Sakar, M.; Katapadi, M.; Balakrishna, R. G. Recent case studies on the use of ozone to combat coronavirus: problems and perspectives. *Environ. Technol. Innov.* **2021**, *21*, 101313.
(48) Zhu, H. Q.; Yu, D. D.; Zhang, X. M. The spike protein of murine coronavirus regulates viral genome transport from the cell surface to the endoplasmic reticulum during infection. *J. Virol.* **2009**, *83*, 10653−10663.
(49) Zhao, Z. Z.; Qin, P.; Huang, Y. W. Lysosomal ion channels involved in cellular entry and uncoating of enveloped viruses: implications for therapeutic strategies against SARS-CoV-2. *Cell Calcium* **2021**, *94*, 102360.
(50) Dalle-Donne, I.; Rossi, R.; Giustarini, D.; Milzani, A.; Colombo, R. Protein carbonyl groups as biomarkers of oxidative stress. *Clin. Chim. Acta* **2003**, *329*, 23−38.
(51) Di Mascio, P.; Martinez, G. R.; Miyamoto, S.; Ronsein, G. E.; Medeiros, M. H. G.; Cadet, J. Singlet molecular oxygen reactions with nucleic acids, lipids, and proteins. *Chem. Rev.* **2019**, *119*, 2043−2086.
(52) Davies, M. J. Singlet oxygen-mediated damage to proteins and its consequences. *Biochem. Biophys. Res. Commun.* **2003**, *305*, 761−770.
(53) Requena, J. R.; Chao, C. C.; Levine, R. L.; Stadtman, E. R. Glutamic and aminoadipic semialdehydes are the main carbonyl products of metal-catalyzed oxidation of proteins. *Proc. Natl. Acad. Sci. U.S.A.* **2001**, *98*, 69−74.
(54) Yang, Y.; Banerjee, G.; Brudvig, G. W.; Kim, J. H.; Pignatello, J. J. Oxidation of organic compounds in water by unactivated peroxymonosulfate. *Environ. Sci. Technol.* **2018**, *52*, 5911−5919.
(55) Jeong, H.; Lee, J. J.; Lee, J.; Na, K. A multiligand architectural photosensitizer that targets hemagglutinin on envelope of influenza virus for photodynamic inactivation. *Small* **2020**, *16*, 2000556.
(56) Foret, M. K.; Lincoln, R.; Do Carmo, S.; Cuello, A. C.; Cosa, G. Connecting the ″Dots″: from free radical lipid autoxidation to cell pathology and disease. *Chem. Rev.* **2020**, *120*, 12757−12787.
(57) Ryu, W.-S. Virus life cycle. In *Molecular Virology of Human Pathogenic Viruses*, 2017; pp 31−45.

https://doi.org/10.1021/acs.est.3c00163
Environ. Sci. Technol. XXXX, XXX, XXX−XXX

(58) Wigginton, K. R.; Kohn, T. Virus disinfection mechanisms: the role of virus composition, structure, and function. *Curr. Opin. Virol.* **2012**, *2*, 84−89.
(59) Bosch, B. J.; van der Zee, R.; de Haan, C. A. M.; Rottier, P. J. M. The coronavirus spike protein is a class I virus fusion protein: Structural and functional characterization of the fusion core complex. *J. Virol.* **2003**, *77*, 8801−8811.
(60) Zelus, B. D.; Schickli, J. H.; Blau, D. M.; Weiss, S. R.; Holmes, K. V. Conformational changes in the spike glycoprotein of murine coronavirus are induced at 37 degrees C either by soluble murine CEACAM1 receptors or by pH 8. *J. Virol.* **2003**, *77*, 830−840.
(61) Peng, G. Q.; Sun, D. W.; Rajashankar, K. R.; Qian, Z. H.; Holmes, K. V.; Li, F. Crystal structure of mouse coronavirus receptor-binding domain complexed with its murine receptor. *Proc. Natl. Acad. Sci. U.S.A.* **2011**, *108*, 10696−10701.
(62) Mi, D.; Ou, X. Y.; Li, P.; Peng, G. Q.; Liu, Y.; Guo, R. X.; Mu, Z. X.; Li, F.; Holmes, K.; Qian, Z. H. Glycine 29 Is critical for conformational changes of the spike glycoprotein of mouse hepatitis virus A59 triggered by either receptor binding or high pH. *J. Virol.* **2019**, *93*, e01046-19.
(63) Ruiz, M.; Yang, Y.; Lochbaum, C. A.; Delafield, D. G.; Pignatello, J. J.; Li, L. J.; Pedersen, J. A. Peroxymonosulfate oxidizes amino acids in water without activation. *Environ. Sci. Technol.* **2019**, *53*, 10845−10854.
(64) Stadtman, E. R.; Van Remmen, H.; Richardson, A.; Wehr, N. B.; Levine, R. L. Methionine oxidation and aging. *Biochim. Biophys. Acta, Proteins Proteomics* **2005**, *1703*, 135−140.
(65) Xu, Y. H.; Liu, Y. W.; Lou, Z. Y.; Qin, L.; Li, X.; Bai, Z. H.; Pang, H.; Tien, P.; Gao, G. F.; Rao, Z. Structural basis for coronavirus-mediated membrane fusion: crystal structure of mouse hepatitis virus spike protein fusion core. *J. Biol. Chem.* **2004**, *279*, 30514−30522.
(66) Walls, A. C.; Tortorici, M. A.; Snijder, J.; Xiong, X. L.; Bosch, B. J.; Rey, F. A.; Veesler, D. Tectonic conformational changes of a coronavirus spike glycoprotein promote membrane fusion. *Proc. Natl. Acad. Sci. U.S.A.* **2017**, *114*, 11157−11162.
(67) Dirac, P. A. M. The quantum theory of the emission and absorption of radiation. *Proc. R. Soc. A: Math. Phys. Eng. Sci.* **1927**, *114*, 243−265.
(68) Zhan, C.-G.; Dixon, D. A. The nature and absolute hydration free energy of the solvated electron in water. *J. Phys. Chem. B* **2003**, *107*, 4403−4417.
(69) Hai, X.; Xi, S. B.; Mitchell, S.; Harrath, K.; Xu, H. M.; Akl, D. F.; Kong, D. B.; Li, J.; Li, Z. J.; Sun, T.; Yang, H. M.; Cui, Y. G.; Su, C. L.; Zhao, X. X.; Li, J.; Perez-Ramirez, J.; Lu, J. Scalable two-step annealing method for preparing ultra-high-density single-atom catalyst libraries. *Nat. Nanotechnol.* **2022**, *17*, 174−181.

https://doi.org/10.1021/acs.est.3c00163
Environ. Sci. Technol. XXXX, XXX, XXX−XXX